Quantum-State Resolved Bimolecular Collisions of Velocity-Controlled OH with NO Radicals

Moritz Kirste *et al.*

Science **338**, 1060 (2012);
DOI: 10.1126/science.1229549

32. R. Kumar, C. E. Wyman, *Biotechnol. Bioeng.* **102**, 1544 (2009).
33. C. X. Fu *et al.*, *Proc. Natl. Acad. Sci. U.S.A.* **108**, 3803 (2011).
34. F. Chen, R. A. Dixon, *Nat. Biotechnol.* **25**, 759 (2007).
35. F. Chen, Y. Tobimatsu, D. Havkin-Frenkel, R. A. Dixon, J. Ralph, *Proc. Natl. Acad. Sci. U.S.A.* **109**, 1772 (2012).

Acknowledgments: We thank M. P. Tucker for the fungal cellulases; S. Xie for guidance regarding SRS microscopy; K. Ruckman for manuscript editing; and A. J. Ragauskas, C. E. Wyman, M. F. Davis, D. J. Johnson, and R. H. Atalla for valuable discussion. This work was supported by the U.S. Department of Energy (DOE) under contract no. DE-AC36-08-GO28308 with the National Renewable Energy Laboratory. We acknowledge research support from the BioEnergy Science Center, a DOE Bioenergy Research Center, and the Genomic Science Program (ER65258), both supported by the Office of Biological and Environmental Research in the DOE Office of Science. S.-Y.D. conceptualized the project, conducted AFM, analyzed the data, and wrote the manuscript. Y.-S.L. conducted enzyme labeling, bright-field light microscopy, and CLSM. Y.Z. conducted SRS microscopy. E.A.B. purified the cellulosomes. S.-Y.D., M.E.H., J.O.B., and E.A.B. revised the manuscript. We declare no competing financial interests.

Supplementary Materials
www.sciencemag.org/cgi/content/full/338/6110/1055/DC1
Materials and Methods
Figs. S1 to S8
References (*36*–*40*)
Movies S1 to S4

16 July 2012; accepted 21 September 2012
10.1126/science.1227491

Quantum-State Resolved Bimolecular Collisions of Velocity-Controlled OH with NO Radicals

Moritz Kirste,[1]* Xingan Wang,[1]* H. Christian Schewe,[1] Gerard Meijer,[1] Kopin Liu,[2] Ad van der Avoird,[3] Liesbeth M. C. Janssen,[3] Koos B. Gubbels,[3] Gerrit C. Groenenboom,[3]† Sebastiaan Y. T. van de Meerakker[3,1]†

Whereas atom-molecule collisions have been studied with complete quantum-state resolution, interactions between two state-selected molecules have proven much harder to probe. Here, we report the measurement of state-resolved inelastic scattering cross sections for collisions between two open-shell molecules that are both prepared in a single quantum state. Stark-decelerated hydroxyl (OH) radicals were scattered with hexapole-focused nitric oxide (NO) radicals in a crossed-beam configuration. Rotationally and spin-orbit inelastic scattering cross sections were measured on an absolute scale for collision energies between 70 and 300 cm^{-1}. These cross sections show fair agreement with quantum coupled-channels calculations using a set of coupled model potential energy surfaces based on ab initio calculations for the long-range nonadiabatic interactions and a simplistic short-range interaction. This comparison reveals the crucial role of electrostatic forces in complex molecular collision processes.

Rotationally inelastic scattering is one of the key processes underlying the exchange of energy between molecules (*1*, *2*). In bulk systems, rotational energy transfer (RET) is responsible for the thermalization of state populations after a chemical reaction. In the dilute interstellar medium, inelastic collisions contribute to the formation of nonthermal population distributions that result in, for instance, interstellar masers (*3*). Accurate state-to-state inelastic scattering cross sections are essential ingredients for reliable models of chemical processes in combustion physics, atmospheric science, and astrochemistry.

In molecular beam collision experiments, the ability to prepare molecules in a single rotational (sub)level before the collision using electric, magnetic, or optical fields has been imperative to unravel the underlying mechanisms of molecular energy transfer. This has made scattering experiments possible at the full state-to-state level and has resulted in the discovery of propensity rules for inelastic scattering (*4*), the stereodynamics of molecular collisions (*5*, *6*), and quantum interference effects (*7*–*9*). The latest beam deceleration and acceleration methods (*10*, *11*) allow for the precise variation of the collision energy, resulting in the observation of quantum threshold effects in the state-to-state cross sections (*12*, *13*). This wealth of studies has contributed enormously to our present understanding of how intermolecular potentials govern molecular collision dynamics.

Thus far, these methods have mostly been used to study collisions of state-selected molecules with rare gas atoms. Yet, in most natural environments, molecule-molecule interactions play a major role. For instance, space telescope observations of cometary water may reveal the possible origin of water on Earth, but a conclusive interpretation requires accurate knowledge of RET in water-water collisions (*14*). Whereas atom-molecule scattering cross sections can now be calculated routinely in excellent agreement with experiment (*13*, *15*), much less is known about RET in molecule-molecule collisions (*16*). As opposed to an atomic target, a molecular scattering partner possesses internal degrees of freedom of its own, adding a level of complexity that can easily render ab initio quantum scattering calculations extremely challenging, if not impossible. This is particularly true for collisions involving radical species that are governed by multiple Born-Oppenheimer (BO) potential energy surfaces (PESs) with nonadiabatic couplings between them. Experimental data on bimolecular state-to-state cross sections is generally lacking, and kinetic models often use collision rate coefficients that are expected to be inaccurate (*17*).

The study of molecule-molecule collisions at the ultimate quantum level has been a quest in molecular beam physics since it was established in the 1950s (*18*). Major obstacles exist that have prevented studies of state-to-state bimolecular scattering (*19*). The main challenge is the need for reagent beams with sufficient quantum-state purity at the densities necessary to observe population transfer in one, or both, reagent beam(s). Thus far, experiments of this kind have only been possible using cryogenically cooled H_2 molecules as a target beam (*20*, *21*).

Here, we report the successful measurement of state-resolved inelastic scattering between two state-selected molecular beams. We have chosen the OH ($X\,^2\Pi$) + NO ($X\,^2\Pi$) system (*22*) for this purpose, as both open-shell radical species are benchmark systems for the scattering of state-selected molecules with rare gas atoms that involve two BO PESs (*23*). Collisions between OH and NO involve eight interacting PESs, representing the full complexity of bimolecular inelastic collisions (*24*). The OH-NO system serves also as a prototypical example of radical-radical reactions of fundamental importance in gas-phase chemical kinetics (*25*). We used a Stark decelerator and a hexapole state selector in a crossed molecular beam configuration to produce reagent beams of OH and NO radicals with an almost perfect quantum-state purity. The collision energy was varied between 70 and 300 cm^{-1} by tuning the velocity of the OH radicals before the collision using the Stark decelerator, revealing the quantum threshold behavior of the state-to-state inelastic scattering cross sections. The unusually well-defined distributions of reagent molecules allowed us to determine absolute scattering cross sections, which can normally be determined only on a relative scale in crossed-beam experiments. These cross sections showed fair agreement with a theoretical model for inelastic collisions between two $^2\Pi$ radical species, based solely on an accurate description of the full rotational and open-shell structure of both

[1]Fritz-Haber-Institut der Max-Planck-Gesellschaft, Faradayweg 4-6, 14195 Berlin, Germany. [2]Institute of Atomic and Molecular Sciences (IAMS), Academia Sinica, Taipei, Taiwan 10617. [3]Radboud University Nijmegen, Institute for Molecules and Materials, Heijendaalseweg 135, 6525 AJ Nijmegen, The Netherlands.

*These authors contributed equally to this work.
†To whom correspondence should be addressed. E-mail: basvdm@science.ru.nl (S.Y.T.v.d.M.), gerritg@theochem.ru.nl (G.C.G.)

radical species and their long-range nonadiabatic electrostatic interactions. This study revealed that inelastic scattering predominantly occurs at large intermolecular distances, even for the relatively high collision energies probed here.

The crossed molecular beam apparatus used to study inelastic collisions between OH and NO radicals is schematically shown in Fig. 1 (*26*). A packet of OH radicals [$X\,^2\Pi_{3/2}$, $v = 0$, $j = 3/2$, f (*22*), referred to hereafter as $F_1(3/2f)$] with a tunable velocity in the 200 to 750 m/s range was produced using a 2.6-m long Stark decelerator (*27*). The velocity of the OH radicals was tuned by applying a burst of high-voltage pulses to the electric field electrodes at the appropriate times. The state purity of the OH packets was such that less than 0.01% of the OH radicals populated a lower Λ-doublet component of any rotational level.

A beam of NO radicals with a fixed velocity was produced by seeding NO in a xenon carrier gas and was passed through a 30-cm-long electrostatic hexapole. NO radicals in the low-field-seeking $F_1(1/2f)$ state were focused into the collision region, whereas molecules in the high-field-seeking $F_1(1/2e)$ state were deflected from the beam axis. A 2-mm-diameter beamstop and diaphragm were installed in the center of the hexapole and 10 mm downstream from the hexapole, respectively, effectively filtering out the Xe atoms from the molecular beam pulse. The resulting state purity of the transmitted NO $F_1(1/2f)$ beam was better than 99.0%.

The reagent beams of OH and NO were detected state-selectively in the collision region by a laser-induced fluorescence (LIF) detection scheme. From calibrated LIF measurements, the peak densities of the reagent packets were determined to be $(2 \pm 0.8) \times 10^8$ and $(9 \pm 3) \times 10^{10}$ molecules/cm^3 for OH and NO, respectively. The collision-induced populations in the $F_1(3/2e)$, $F_1(5/2e)$, $F_1(7/2e)$, and $F_2(1/2e)$ levels of the OH radical were measured at the time when both beams maximally overlapped in the beam-crossing area. Depending on the inelastic channel, only a fraction of 10^{-4} to 10^{-6} of the OH radicals were inelastically scattered. Only final states of e symmetry were probed, as the Stark decelerator did not eliminate the initial population in the f states sufficiently. Detection of collision-induced population in the $F_1(3/2e)$ level was only possible by spectroscopically separating the magnetic dipole–allowed transitions that originated from the $F_1(3/2f)$ state (*26*). The insufficiently perfect state purity of the NO radical beam prevented the measurement of population transfer in NO.

The collision signals were measured as a function of the collision energy, from which the excitation functions of the state-to-state inelastic scattering cross sections (shown in Fig. 2) were determined (*28*). The extremely well-defined spatial distributions of the OH and NO packets allowed us to determine the scattering cross sections on an absolute scale. A cross section of 90 ± 38 Å^2 was determined for the $F_1(3/2e)$ channel at a collision energy of 220 cm^{-1}, from which the absolute cross sections for all scattering channels and all collision energies were derived (*26*). The experimental uncertainty was limited only by the uncertainty in the measured value for the peak density of the NO packet.

We found that collisions that populate the $F_1(3/2e)$ level are most likely, and the cross section for this transition accounts for about 90% of the total inelastic scattering cross section. The cross sections to populate the $F_1(5/2e)$, the $F_1(7/2e)$, and the $F_2(1/2e)$ levels show a clear threshold behavior; the collision energies at which these channels become energetically possible are indicated by vertical arrows. These cross sections show large qualitative differences compared with the scattering of OH with atomic targets. The most striking difference is found in the relative contributions of the $F_1(3/2e)$ and $F_1(5/2e)$ channels to the total inelastic scattering cross section. The role of the $F_1(5/2e)$ channel, which dominates RET for OH-He and OH-Ne, gradually diminishes in favor of the $F_1(3/2e)$ channel in the series of targets He, Ne, Ar, Kr, and Xe (*29*). This behavior could be rationalized from the increasing well depth, anisotropy, and head-tail asymmetry of the two BO PESs (*29*, *30*). The overwhelming dominance of the $F_1(3/2f) \rightarrow F_1(3/2e)$ quenching channel observed here for OH-NO reflects how a dipolar open-shell molecular scattering partner, rather than a spherical atomic partner, governs the collision dynamics.

To interpret our experimental results, we constructed a model for the scattering of two molecules in an open-shell $^2\Pi$ state. In contrast to scattering of OH or NO with rare gas atoms, ab initio calculations of multiple anisotropic PESs with their nonadiabatic couplings for OH-NO are beyond the capabilities of current theoretical methods. Coupling of the $S = 1/2$ electron spins gives rise to singlet ($S = 0$) and triplet ($S = 1$) potentials, which describe different short-range exchange interactions. There are four spatially distinct electronic states for each spin state, which are degenerate at long range and for linear geometries and which are coupled by nonadiabatic interactions. Nuclear derivative couplings with respect to all nuclear degrees of freedom exist between these states. Ab initio studies of the OH-NO complex (*31*) focused on the region where the chemical reaction OH + NO → H + NO_2 takes place but considered only the lowest adiabatic potential for the singlet state. Even if we were able to compute all the relevant adiabatic PESs, there would be no simple recipe to take the nonadiabatic couplings between the PESs into account.

In our model, we exploit the hypothesis that the processes with the largest cross sections are governed by couplings that occur at relatively large OH-NO separations, beyond the HONO well region. As opposed to the short-range interactions, the long-range parts of the PESs can be calculated accurately by ab initio methods. We neglected the complicated short-range behavior of the PESs and replaced it with an isotropic repulsion term. However, we accurately calculated the long-range PESs that are governed by first-order electrostatic interactions between the dipole, quadrupole, and octupole moments of the

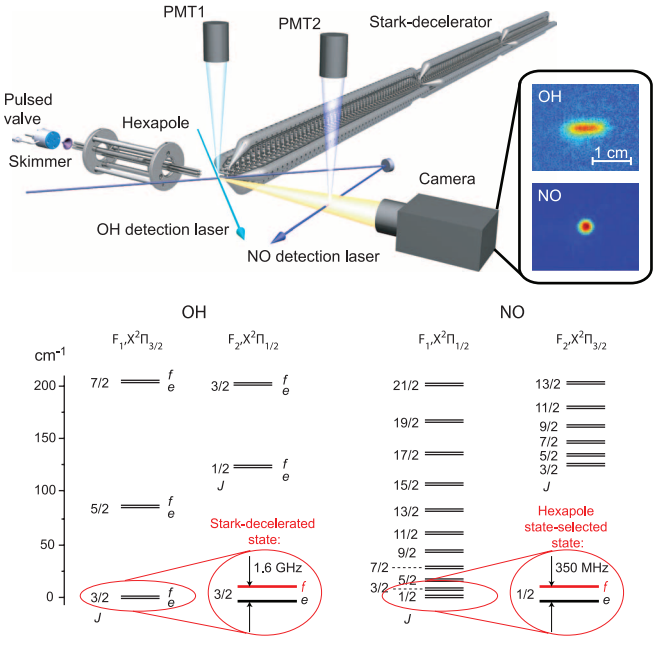

Fig. 1. Schematic representation of the experimental setup and the energy level schemes of the OH and NO radicals. A state-selected and velocity tunable beam of OH radicals produced using a 2.6-m-long Stark decelerator was crossed with a hexapole state-selected beam of NO radicals. Both radical species were detected state-selectively using LIF, with total fluorescence intensity measured using a photomultiplier tube (PMT), and the spatial distributions of both reagent molecular packets were imaged onto a charge-coupled device camera. Typical images of the OH and NO packets are shown in the upper and lower insets, respectively. The mean speed of the OH radical packet was precisely known from the settings of the Stark decelerator. The collision energy was calibrated from the NO beam speed measured by a second LIF detection zone located 30 cm downstream from the collision area. The $X\,^2\Pi$ electronic ground states of the OH and NO radicals are split into two rotational manifolds due to the spin-orbit interaction. The manifolds with lowest energy [$|\Omega| = 3/2$ for OH and $|\Omega| = 1/2$ for NO] are labeled F_1. The energy splittings shown between the Λ-doublet components of each rotational level are greatly exaggerated for clarity.

collision partners (*26*). Moreover, we included isotropic dispersion and induction terms. The intermolecular Hamiltonian contained the usual radial and centrifugal kinetic energy operators and the full 4 × 4 matrix of diabatic interaction potentials (*26*, *32*). Due to the noncylindrical symmetry of the $^2\Pi$ ground states of both the OH and NO radical, the off-diagonal elements of this matrix provided by the quadrupole and octupole moments of both radicals contain important couplings between the $^2\Pi_{3/2}$ and $^2\Pi_{1/2}$ states of both species.

The cross sections that were obtained from these model PESs by full coupled-channels calculations are shown as solid lines in Fig. 2. Fair agreement between experiment and theory was obtained, in particular considering the simplistic approximations for the short-range PESs that were made. The absolute value for the cross section of the dominating $F_1(3/2e)$ channel, as well as the relative strengths of the inelastic channels, are reproduced well by the model calculations. The cross section for the spin-orbit–changing $F_2(1/2e)$ channel, as well as the cross section for the $F_1(3/2e)$ channel at low collision energies, are overestimated by the model.

We tested the sensitivity of the model calculations with respect to changes in the short-range repulsion term (*26*). We observed that the cross section for the parity-changing $F_1(3/2e)$ channel is governed exclusively by the long-range electrostatic interaction; its value is converged to within a few percent. About half of this large quenching cross section originates from collisions with impact parameters exceeding 12 a_0. The $F_1(5/2e)$ channel is also mainly determined by the long-range forces, although its cross section varies by 10 to 25% upon changes in the short-range model parameters (*26*). The weak $F_1(7/2e)$ and $F_2(1/2e)$ channels show larger variations, and more realistic short-range PESs are required to accurately predict their cross sections.

Our model also predicts the final states of the NO radical that are populated in coincidence with RET in the OH radical but that cannot be probed with the present experimental arrangement. The dominant $F_1(3/2e)$ quenching transition in OH is accompanied by the inelastic channels in NO as given in Table 1 for various collision energies. The general scattering behavior can be understood from the terms that lead to inversion parity changing or conserving collisions with respect to both collision partners. The OH-NO dipole-dipole interaction results in transitions that either change or conserve inversion parity in both OH and NO, whereas the dipole-quadrupole and quadrupole-dipole terms also allow for an inversion parity changing transition in OH or NO only. The largest cross sections that accompany the $F_1(3/2e)$ channel in OH are found for the dipole-dipole–dominated $F_1(3/2f)$ and $F_1(1/2e)$ channels of NO and for the dipole-quadrupole dominated $F_1(1/2f)$, $F_1(3/2e)$, and $F_1(5/2f)$ NO channels (*33*).

Our experiments show that the main mechanisms of RET in the reactive, chemically complex system studied here are captured using a model for the long-range interactions alone, provided that the full monomer Hamiltonians and all relevant long-range nonadiabatic couplings are taken into account. Even at relatively high collision energies, the inelastic scattering events with the largest cross sections predominantly occur at large intermolecular distances where the interaction potentials can be calculated accurately. The success attained here implies that reliable predictions for state-to-state scattering cross sections can now be made more generally for complex molecular systems involving radicals, helping to solve urgent scientific questions in, for instance, astrochemistry. Ultimately, new electronic structure methods that include the chemically reactive short-range potentials and nonadiabatic couplings are required to elucidate the exact mechanisms of radical-radical collisions.

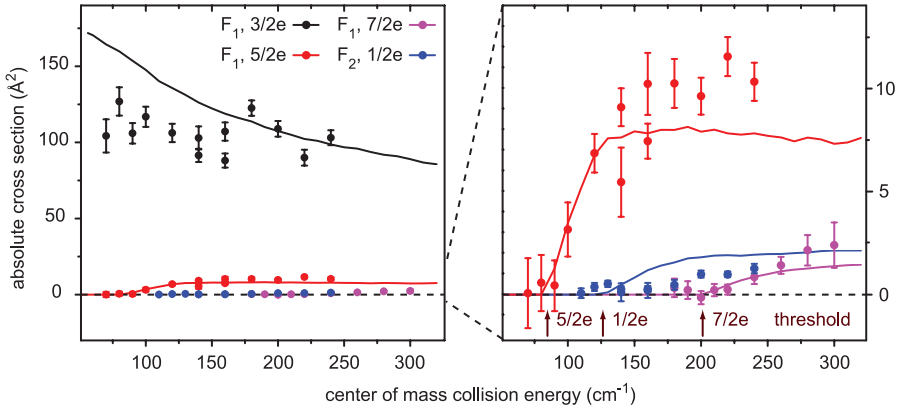

Fig. 2. Comparison of the collision-energy dependence of the measured (data points with error bars) and calculated (solid curves) state-to-state inelastic scattering cross sections of OH $F_1(3/2f)$ radicals in collision with NO $F_1(1/2f)$ radicals. The cross sections were first measured relatively with respect to each other, and the vertical error bars indicate combined estimates of both statistical and systematic errors (2 SD) (*26*). The vertical axis was then put on an absolute scale by a measurement of the absolute cross section for the $F_1(3/2e)$ channel at a collision energy of 220 cm^{-1}. The cross sections were computed on an energy grid of 10, 20, 30, 40, ..., 320 cm^{-1}. The cross section for the dominant $F_1(3/2e)$ channel converged to within a few percent; the cross sections for the weaker channels vary by 20 to 50% depending on changes in the short-range part of the theoretical model (*26*).

Table 1. Predicted state-to-state cross sections (Å^2) for RET in NO [initial state $F_1(1/2f)$] that occurs in coincidence with the $F_1(3/2f) \rightarrow F_1(3/2e)$ transition in the OH radical at collision energies of 10, 20, 50, 100, 200, and 300 cm^{-1}. The inversion parity of the molecular levels is given. For comparison, the elastic cross section corresponding to the OH [$F_1(3/2f) \rightarrow F_1(3/2f)$] – NO [$F_1(1/2f) \rightarrow F_1(1/2f)$] channel is given in the last row of the table.

Final state (NO)	Inversion parity	10 cm^{-1}	20 cm^{-1}	50 cm^{-1}	100 cm^{-1}	200 cm^{-1}	300 cm^{-1}
$F_1(1/2e)$	+	152.3	106.6	54.5	33.5	20.0	15.3
$F_1(1/2f)$	–	45.1	37.0	25.8	13.9	6.3	4.2
$F_1(3/2e)$	–	19.1	17.6	21.4	17.5	12.1	10.0
$F_1(3/2f)$	+	18.0	19.5	46.9	54.3	38.8	29.7
$F_1(5/2e)$	+		6.5	8.5	9.0	6.3	5.0
$F_1(5/2f)$	–		6.6	7.1	8.7	11.8	13.4
$F_1(7/2e)$	–			5.3	5.4	4.4	3.8
$F_1(7/2f)$	+			4.7	5.2	5.6	5.6
$F_2(3/2e)$	–					0.5	0.4
$F_2(3/2f)$	+					0.5	0.4
$F_2(5/2e)$	+					0.4	0.3
$F_2(5/2f)$	–					0.4	0.4
$F_2(7/2e)$	–					0.3	0.3
$F_2(7/2f)$	+					0.3	0.3
Elastic		409.6	346.3	265.1	209.1	175.8	166.4

References and Notes

1. R. D. Levine, R. B. Bernstein, *Molecular Reaction Dynamics and Chemical Reactivity* (Oxford University Press, New York, 1987).
2. D. W. Chandler, S. Stolte, in *Tutorials in Molecular Reaction Dynamics*, M. Brouard, C. Vallance, Eds. (Royal Society of Chemistry, Cambridge, 2010), chap. 5.
3. S. Weinreb, A. H. Barrett, M. L. Meeks, J. C. Henry, *Nature* **200**, 829 (1963).

4. A. Schiffman, D. W. Chandler, *Int. Rev. Phys. Chem.* **14**, 371 (1995).
5. S. Stolte, *Nature* **353**, 391 (1991).
6. D. Watanabe, H. Ohoyama, T. Matsumura, T. Kasai, *Phys. Rev. Lett.* **99**, 043201 (2007).
7. K. T. Lorenz *et al.*, *Science* **293**, 2063 (2001).
8. C. J. Eyles *et al.*, *Nat. Chem.* **3**, 597 (2011).
9. H. Kohguchi, T. Suzuki, M. H. Alexander, *Science* **294**, 832 (2001).
10. S. Y. T. van de Meerakker, H. L. Bethlem, G. Meijer, *Nat. Phys.* **4**, 595 (2008).
11. S. Y. T. van de Meerakker, H. L. Bethlem, N. Vanhaecke, G. Meijer, *Chem. Rev.* **112**, 4828 (2012).
12. J. J. Gilijamse, S. Hoekstra, S. Y. T. van de Meerakker, G. C. Groenenboom, G. Meijer, *Science* **313**, 1617 (2006).
13. L. Scharfenberg *et al.*, *Phys. Chem. Chem. Phys.* **12**, 10660 (2010).
14. P. Hartogh *et al.*, *Nature* **478**, 218 (2011).
15. G. Paterson, M. L. Costen, K. G. McKendrick, *Int. Rev. Phys. Chem.* **31**, 69 (2012).
16. D. C. Clary, *Annu. Rev. Phys. Chem.* **41**, 61 (1990).
17. I. W. M. Smith, *Annu. Rev. Astron. Astrophys.* **49**, 29 (2011).
18. R. B. Bernstein, *Science* **144**, 141 (1964).
19. B. C. Sawyer *et al.*, *Phys. Chem. Chem. Phys.* **13**, 19059 (2011).
20. C. Berteloite *et al.*, *Phys. Rev. Lett.* **105**, 203201 (2010).
21. K. Schreel, J. J. ter Meulen, *J. Chem. Phys.* **105**, 4522 (1996).
22. The labels $X^2\Pi_{3/2}$, $X^2\Pi_{1/2}$, v, and j indicate the electronic states, the vibrational state, and the rotational state of both the OH and the NO radical, respectively. The spectroscopic symmetry labels e and f refer to the total parity of the electronic wave function, exclusive of rotation. The total inversion parity is indicated by the additional labels + and −.
23. H. Kohguchi, T. Suzuki, *Annu. Rep. Prog. Chem. Sect. C* **98**, 421 (2002).
24. M. T. Vonk, J. A. Bacon, C. F. Giese, W. R. Gentry, *J. Chem. Phys.* **106**, 1353 (1997).
25. P. Sharkey, I. R. Sims, I. W. M. Smith, P. Bocherel, B. R. Rowe, *J. Chem. Soc. Faraday Trans.* **90**, 3609 (1994).
26. Materials and methods are available as supplementary materials on *Science* Online.
27. L. Scharfenberg, H. Haak, G. Meijer, S. Y. T. van de Meerakker, *Phys. Rev. A* **79**, 023410 (2009).
28. It was verified that all scattered molecules are detected with equal probability, and no density-to-flux correction was needed to relate the measured scattering signals to relative inelastic cross sections. See supplementary materials for more information.
29. L. Scharfenberg *et al.*, *Eur. Phys. J. D* **65**, 189 (2011).
30. P. J. Dagdigian, M. H. Alexander, *J. Chem. Phys.* **130**, 094303 (2009).
31. M. T. Nguyen, R. Sumathi, D. Sengupta, J. Peeters, *Chem. Phys.* **230**, 1 (1998).
32. The OH-NO spin states with $S = 0$ and $S = 1$ are not distinguished in our model; the 4 × 4 matrices for each spin state are therefore identical.
33. Although the quadrupole moment vanishes in the $j = 1/2$ state of NO, the quadrupole moment in the molecular frame contributes to the collisions producing NO states with $j = 3/2$ and 5/2 that yield important contributions to the measured cross sections.

Acknowledgments: S.Y.T.v.d.M. acknowledges support from the Netherlands Organisation for Scientific Research (NWO) via a VIDI grant. G.M. and K.B.G. acknowledge support from the ERC-2009-AdG under grant agreement 247142-MolChip. K.L. and A.v.d.A. acknowledge the Alexander von Humboldt Foundation (AvHF) for a Humboldt Research Award. X.W. acknowledges the AvHF for a research fellowship. We thank J. Blokland for her help setting up the narrowband laser system. We thank the referees for valuable and stimulating comments. The authors declare no competing financial interests.

Supplementary Materials

www.sciencemag.org/cgi/content/full/338/6110/1060/DC1
Supplementary Text
Figs. S1 to S3
Tables S1 and S2
References (*34*–*49*)

19 June 2012; accepted 10 October 2012
10.1126/science.1229549

Body-Wave Imaging of Earth's Mantle Discontinuities from Ambient Seismic Noise

P. Poli,* M. Campillo, H. Pedersen, LAPNET Working Group

Ambient seismic noise correlations are widely used for high-resolution surface-wave imaging of Earth's lithosphere. Similar observations of the seismic body waves that propagate through the interior of Earth would provide a window into the deep Earth. We report the observation of the mantle transition zone through noise correlations of *P* waves as they are reflected by the discontinuities associated with the top [410 kilometers (km)] and the bottom (660 km) of this zone. Our data demonstrate that high-resolution mapping of the mantle transition zone is possible without using earthquake sources.

Earth's upper and lower mantle are separated by the transition zone, where the mantle mineralogy changes. At the top (~410 km depth) and bottom (~660 km depth) of the transition zone, phase changes introduce a rapid increase in seismic velocities over narrow depth intervals. This transition zone has a major role in Earth dynamics, particularly as it influences the convection within the mantle, slowing the subduction of slabs and the ascent of plumes (*1*, *2*). Information from rock physics and the seismic character of the 410-km and 660-km discontinuities can constrain the mineralogy and temperatures of the mantle (*3*). However, mapping the depths and lateral variations of these discontinuities (*4*, *5*) remains difficult. Seismic studies based on the analysis of waves emitted by earthquakes are limited by the geographical distribution of the earthquakes and by the uncertainties in our knowledge of the location and the rupture processes.

Promising results from correlations of the coda of seismic waves (*6*) have led to the recent proposal that correlations of the continuous records of seismic ambient noise recorded at two distant points can provide an estimation of Earth's impulse response between these two points (*7*). This impulse response contains information on seismic wave speeds (*7*) and amplitude decays (*8*) without the need for the use of active sources or earthquakes. Because these seismic noise sources are located at Earth's surface, the noise correlations are dominated by surface waves, and the technique has become useful for seismic imaging at different scales (*9*–*13*). Seismic noise propagates continuously through Earth and is mainly created by oceanic swells and atmospheric disturbances (*14*–*19*).

Surface waves, however, are not sufficient to explore the deep structure of Earth, as they have limited depth resolution. Recent studies have detected high-frequency body waves within noise correlations at both the crustal scale (*20*–*22*) and at a very local scale (*23*). Here, we describe the use of seismic noise correlations to extract body-wave reflections from the 410-km and 660-km discontinuities of Earth's transition zone.

It is now known that seismic noise includes body waves that propagate through the whole planet (*19*, *24*, *25*), just as surface waves propagate through the upper layers of Earth (Fig. 1A). As for the surface-wave component of the wave field, we do not expect the noise field to be under the exact mathematical conditions for retrieval of the complete Earth impulse responses (*26*, *27*). We show in the following that conditions are nonetheless favorable enough to extract deep body-wave phases by correlating ambient seismic noise. Because the signals we track have small amplitudes, we have applied specific processing techniques that are designed to improve the signal-to-noise ratio.

We used data from the temporary POLENET/LAPNET experiments in northern Finland (*28*) (Fig. 1B), complemented with data from permanent broadband stations. We previously extracted *P* waves and *S* waves (*22*) that are reflected on the Moho (the lower limit of Earth's crust). These data showed that the ancient crust in the study area (*29*, *30*) is relatively transparent to seismic waves. Here, we used data from 42 stations that were continually operating from January to December 2008. For each of the 861 station pairs (fig. S1), we calculated the noise correlation of the vertical records in the frequency range 0.1 to 0.5 Hz, using the same processing as that implemented to extract Moho-reflected waves (*22*). We subsequently used the station pairs for which

Institut des Sciences de la Terre (ISTerre), Université de Grenoble I, CNRS, BP 53, F-38041 Grenoble Cedex 9, France.

*To whom correspondence should be addressed. E-mail: polip@ujf-grenoble.fr